Efficient thermal management of Li-ion batteries with a passive interfacial thermal regulator based on a shape memory alloy

Menglong Hao [1], Jian Li[1,2], Saehong Park [3], Scott Moura[3] and Chris Dames[1,4]*

The poor performance of lithium-ion batteries in extreme temperatures is hindering their wider adoption in the energy sector. A fundamental challenge in battery thermal management systems (BTMSs) is that hot and cold environments pose opposite requirements: thermal transmission at high temperature for battery cooling, and thermal isolation at low temperature to retain the batteries' internally generated heat, leading to an inevitable compromise of either hot or cold performances. Here, we demonstrate a thermal regulator that adjusts its thermal conductance as a function of the temperature, just as desired for the BTMS. Without any external logic control, this thermal regulator increases battery capacity by a factor of 3 at an ambient temperature ($T_{ambient}$) of −20 °C in comparison to a baseline BTMS that is always thermally conducting, while also limiting the battery temperature rise to 5 °C in a very hot environment ($T_{ambient}$ = 45 °C) to ensure safety. The result expands the usability of lithium-ion batteries in extreme environments and opens up new applications of thermally functional devices.

The ongoing transformation of the energy sector to renewables and the advancement of battery technologies have put rechargeable batteries, especially lithium-ion batteries (LIBs), on the centre stage of our future energy landscape. In recent years, the use of LIBs for electric vehicles (EVs), drones and both residential and grid-scale energy storage has been steadily growing, in addition to their growing use in the more established consumer electronics market[1–3]. However, the widespread adoption has been severely hindered by the poor performance of LIBs in both hot and cold climates[4–6]. At high temperatures, batteries degrade at a much higher rate (the lifespan roughly halves for each 13 °C increase in battery temperature[7]), leading to increased cost for replacement[8,9]. When the temperature drops below 15 °C, LIBs suffer from reduced capacity, power and efficiency, which are responsible for a shorter cruise range for EVs and automatic switch-off of smart phones[6,10,11]. Many real-world application scenarios are not in modest conditions[4]. For instance, out of the 51 metropolitan areas (with over 1 million population) in the United States, 20 areas normally experience extreme cold days below −18 °C (0 °F) while the summertime temperatures in 11 areas (including overlaps with the former 20) routinely exceed 38 °C (100 °F)[12]. Maintaining battery temperature within an optimal range regardless of the ambient conditions is vital for the performance of any energy storage system based on LIBs (Fig. 1).

With the modern trend towards fast charging and discharging (that is, higher C rates; 1C rate fully charges/discharges the battery in 1 h), battery thermal management becomes even more challenging. On the one hand, batteries lose power capability at low temperature, making it even more difficult to achieve high C rates. Recent studies have shown that internal heating can quickly warm up LIBs and restore power[13,14]. For this strategy to work, however, good thermal insulation must be in place to prevent the heat from simply leaking away to the ambient[14,15]. On the other hand, high C rates substantially increase heat generation within the battery. Keyser et al. estimate that extreme fast charging (5C or higher), which allows EVs to be charged as fast as conventional vehicles are fuelled and is highly desirable for EV adoption, would raise the battery temperature by more than 200 °C if the pack is not properly heat sunk[7]. A high thermal conductance is therefore critical to avoid batteries overheating in hot ambient. Due to these conflicting requirements for BTMSs (that is, thermal insulation at low temperature and thermal conduction at high temperature), it has been difficult to manage battery temperature for both extreme conditions using traditional linear thermal components (for which the heat flux and the temperature gradient are always linearly proportional). While controlled fluid loops can perform this thermal functionality to some extent (for example, by turning on and off a circulation pump), the ON/OFF contrast is not large enough[16]. In addition, these systems incur higher cost and weight, and are not practical for portable applications.

Here, we report a fluid-free, passive thermal regulator that stabilizes battery temperature in both hot and cold extreme environments. Without any power supply or logic, the thermal regulator switches its thermal conductance according to the local battery temperature and delivers the desirable thermal functionality, retaining heat when it is cold and facilitating cooling when it is hot. Below, we will first introduce the mechanism and demonstrate the performance of the thermal regulator in an ideal vacuum environment. We then apply it for passive thermal management of commercial 18650 LIBs (the most widely used LIB model) in air, over a large range of ambient temperatures from −20 °C to 45 °C.

Thermal regulator design and operating mechanism
The concept of a thermal regulator has existed for decades, but applications have been limited to a few niche markets such as thermal regulation in spaceships[17,18] and cryogenic systems[19], despite growing interest from other fields in recent years[20]. The main issues with current thermal regulators are low switch ratio (SR),
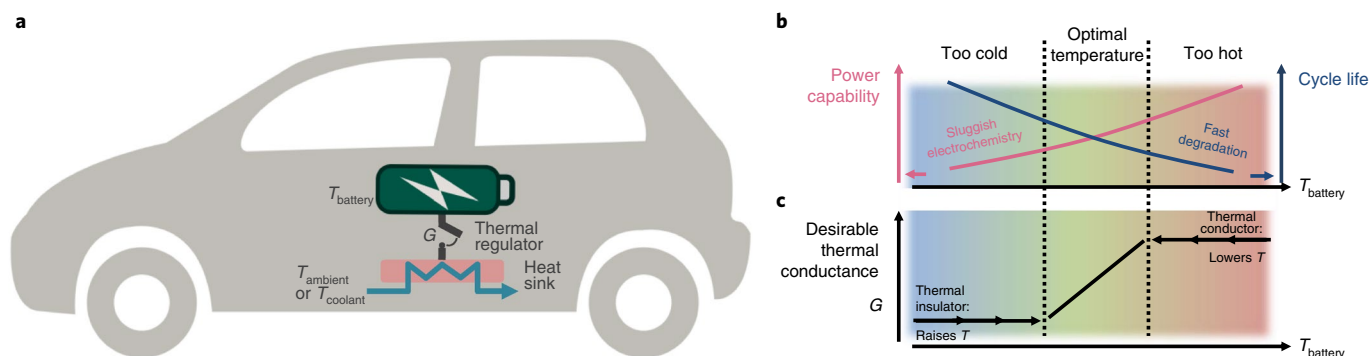
Fig. 1 | A passive thermal regulator concept for battery thermal management. a, A passive thermal regulator is proposed as the thermal link between the battery and its heat sink. **b**, Schematic of temperature trade-offs. Batteries perform poorly at low temperatures due to low power capability and low usable capacity, while high temperatures are harmful to battery lifespan and cause safety issues. **c**, The ideal thermal management strategy should dissipate battery heat to the environment when the battery temperature is too high, and also internally heat and thermally isolate the battery when the battery temperature is too low. Therefore, the ideal thermal regulator for this application should have a high thermal conductance, G, at high temperatures for efficient cooling, and switch to a low G at low temperatures to retain thermal energy and raise the battery temperature.

large footprint, high cost and poor cyclability. The key characteristic of a thermal regulator is a variable thermal conductance as a function of temperature. The SR refers to the ON/OFF thermal conductance ratio and is the most important performance metric for thermal regulators. Many recent developments in the field exploit the jump of thermal conductivity (κ) associated with solid-state phase (or structural) changes, with examples including $Ge_2Sb_2Te_5$ (SR = 8:1, irreversible)[21,22], VO_2 (SR = 1.3:1)[23–25], boron nanoribbons (SR = 1.2:1)[26], $LiCoO_2$ (SR = 1.5:1)[27] and ferroelectric materials, such as $PbZr_{0.3}Ti_{0.7}O_3$ (SR = 1.1:1)[28]. This class of regulators typically exhibit good abruptness (thermal conductance versus temperature approximating a step function rather than a gentle slope) due to the sharp nature of phase change, but have yet to demonstrate a sufficiently high SR for the present battery application. Another class of thermal regulators is based on opening and closing a macroscopic interface, which have shown much higher SR (~100:1 around room temperature) and seen more practical utility[17,18,29]. This type of regulator typically relies on the differential thermal expansion (DTE) between two different materials to induce a geometric change and exploits the strongly nonlinear behaviour of thermal conductance when the interfacial gap closes and becomes a pressure contact. For this class of regulator, the gap size (D) depends on the characteristic length (t) of the thermal regulator body and the actuation strain ($\Delta\varepsilon$) as

$$D \approx \Delta\varepsilon \times t = DTE \times \Delta T \times t \qquad (1)$$

where ΔT is the actuation temperature. However, because thermal expansion is a weak effect (DTE ~ 10^{-5} per degree Celsius), a long thermal regulator body (t ~ 10 cm) is required to close even a small gap of around 0.1 mm[18,29,30]. The cost, weight (80–320 g for a device of 5–6 cm diameter[18,30]) and precision requirements of this thermal regulator outweigh the benefits for mainstream (terrestrial, near room temperature) applications, such as automobiles, drones and portable electronics.

Our approach synergistically integrates the two above-mentioned nonlinearities (that is, solid-state phase change and interfacial thermal contact conductance) in a device topology using shape memory alloy (SMA). SMAs themselves are also phase change materials, and are widely used in biomedical and automotive applications[31]. However, rather than directly utilize the κ change (SR ≈ 1.1:1; ref. [32]) associated with the phase transformation, we take advantage of the change in mechanical properties. Under a constant stress, this translates into changes in the wire strain (typical

reversible $\Delta\varepsilon = 2\%$ over a 20 °C temperature change) and therefore macroscopic displacement. Thus, the average strain response per degree Celsius in an SMA around its transition temperature is ~10^{-3} per degree Celsius, two orders of magnitude larger than that of thermal expansion alone (DTE ~ 10^{-5} per degree Celsius). Due to the SMA's much larger $\partial\varepsilon/\partial T$, the same gap size D can be opened with a much smaller characteristic length t in an SMA thermal regulator than in previous single-phase concepts[18,29]. Despite this improvement, however, to open a gap wide enough (D ~ 0.5 mm) to effectively block heat transfer through air still requires a regulator gauge length of $t = D/\Delta\varepsilon \approx 25$ mm, which is still too large (thicker than an 18650 cell itself) for many automotive and portable electronics applications.

To further amplify the gap closure stroke for a given thermal regulator size (form factor), we developed an SMA actuation configuration whose scaling relation offers an additional degree of freedom beyond the straight-line kinematics of equation (1). As shown schematically in Fig. 2a, thin flexible SMA wires are routed around the thermal regulator and used in tension. In this case, the total wire length is $L \approx 4W + 4t$, and the kinematic relation for gap size becomes

$$D = \frac{\Delta\varepsilon \times L}{4} \approx \Delta\varepsilon \times (W + t) \approx \Delta\varepsilon \times W \qquad (2)$$

where the last step exploits the fact that $W \gg t$. Thus, and in marked contrast to the straight-line scaling of equation (1), the controllable gap size in Fig. 2a is independent of t, allowing for devices with more compact form factors in the cross-gap direction.

We now discuss the thermo-mechanics of a switch-on process in detail, as shown conceptually in Fig. 2b,c. At temperatures below the transition temperature (the typical T_{trans} for Nitinol alloys, metal alloys of nickel and titanium, varies from −15 °C to 80 °C, depending on the Ni/Ti ratio), the bias springs (not shown in Fig. 2a) place the SMA wires in tension, with the static force balance represented by the intersection of the blue and grey curves in Fig. 2b. This defines the 'OFF' state. As the temperature increases, due to the phase transformation the SMA wire gradually starts to strengthen (transitioning from the blue curve to the red curve in Fig. 2b) and contract, pulling the two surfaces closer. This closure process happens in two stages. First, as long as the gap remains finite, the wire stress is counterbalanced by the bias spring force. Therefore, the wire follows the spring's response line (grey) from 'OFF' (blue circle) to 'Touch' (orange circle). During this stage, the contact pressure between the
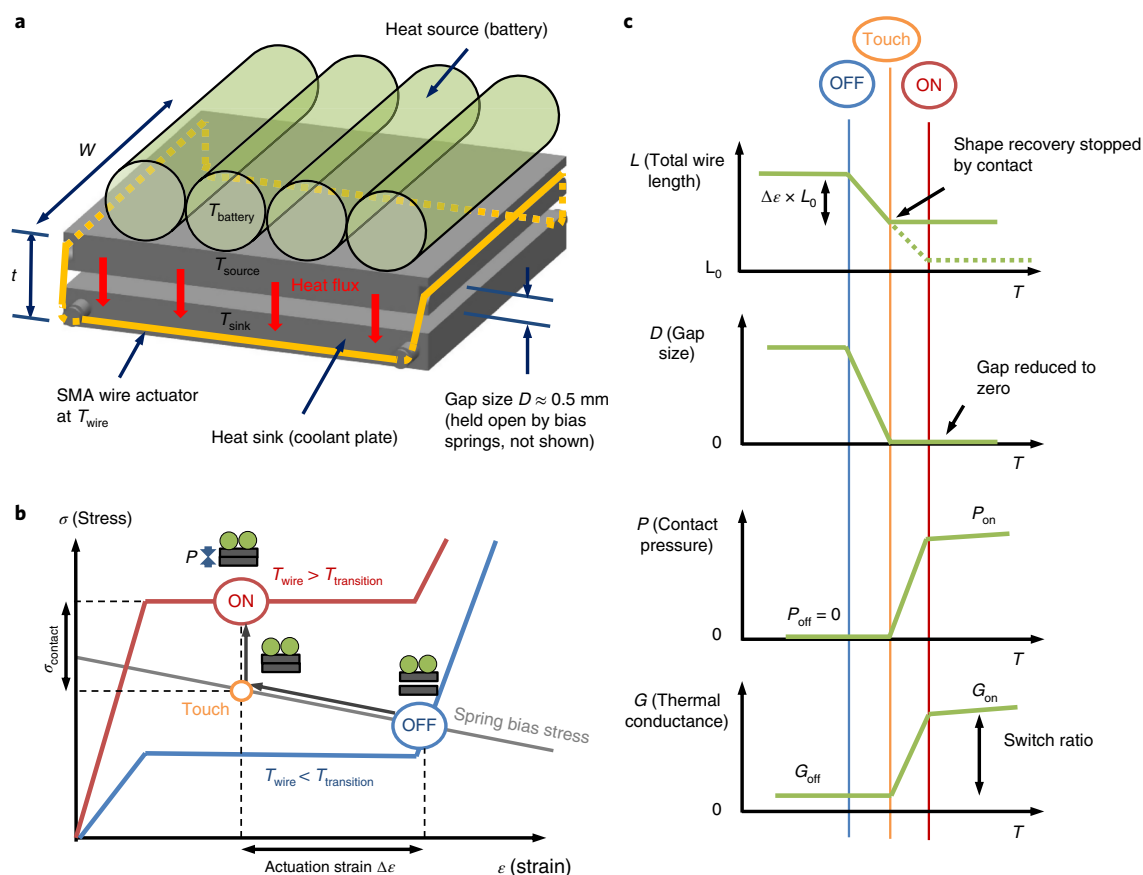
Fig. 2 | Design and switching mechanism of the thermal regulator. a, Design concept for the SMA-actuated thermal regulator. The yellow lines represent the routing of the SMA wire: through the two grooves on the upper plate and around the four low-κ hanger posts on the lower plate, all with sliding contact. This design ensures that T_{wire} is mainly controlled by T_{source} rather than T_{sink}, because the wire has a much larger contact area with the upper plate compared with the lower. As the lateral dimension W of these square plates is fixed, the shape recovery strain of the entire wire length solely manifests as Δt; that is, closing the gap. Bias springs (not shown) separate the two plates at low temperature (OFF mode). **b**, The red and blue lines are conceptual stress–strain curves of Nitinol SMA at temperatures above and below the transition temperature, respectively. The wire switches between ON and OFF points. The grey solid line indicates the stress in the SMA wire at that strain due to the bias spring. Before the gap is completely closed, the forces in the SMA wire and the spring are balanced (neglecting gravity and friction). After the gap is closed (indicated by 'Touch'), the SMA wire cannot get any shorter. Thus, if the temperature keeps rising, the additional force of the SMA wire will be balanced by the contact force between the two surfaces. This contact force gives rise to an abrupt increase in thermal conductance. A thermal interface material (TIM) is used to further enhance the interfacial thermal transport. **c**, The changes to wire length, gap size, contact pressure and thermal conductance during this switching process.

two plates is zero and the thermal conductance through the gap is low. Then the wire reaches the 'Touch' point where the gap closes to zero. Now in the second stage, further wire contraction is prohibited by the two touching surfaces, and further temperature increase results only in stress build-up in the wire. The force exerted by the wire now exceeds the force from the bias springs, with the difference made up by the interface contact force $F = PW^2$, where P is the contact pressure at the interface. This P leads to drastically better interfacial thermal transport[33]. If the SMA temperature continues to increase beyond its transition range, because the phase transformation is finished the thermal regulator maintains this 'ON' state without significant further changes in the mechanics or thermal transport. Clearly, obtaining the highest SR requires optimizing parameters such as wire diameter and length and the bias spring (see Supplementary Information, Note 1 for detailed optimization discussions).

A simple one-dimensional heat transfer model is used to estimate the performance of the thermal regulator. In the OFF state, heat transfer between the two plates occurs via parallel mechanisms of radiation, conduction leakage through the SMA wires (and bias springs), and convection if in air. In the ON state, the direct heat

conduction through the thermal interface material (TIM) dominates the thermal resistance. For the present thermal regulator design in an ideal vacuum environment, the SR is estimated to reach 1,600:1 to 3,200:1 (see Supplementary Note 2 for model details), which is an order of magnitude higher than that of any room-temperature thermal regulator reported to date[18,29,34].

Proof-of-concept test in vacuum

To experimentally validate our thermal model, we designed a test rig modified from the popular ASTM-5470 'reference bar' standard[35,36], as shown in Fig. 3a,c. To measure the thermal contact conductance of the regulator interface, two stainless steel reference bars with thermocouples (calibrated to ±5 mK) are used as a heat source and heat sink. With the temperature profile measured and the stainless steel thermal conductivity well documented from the literature, the heat flux through the bars can be calculated using Fourier's law
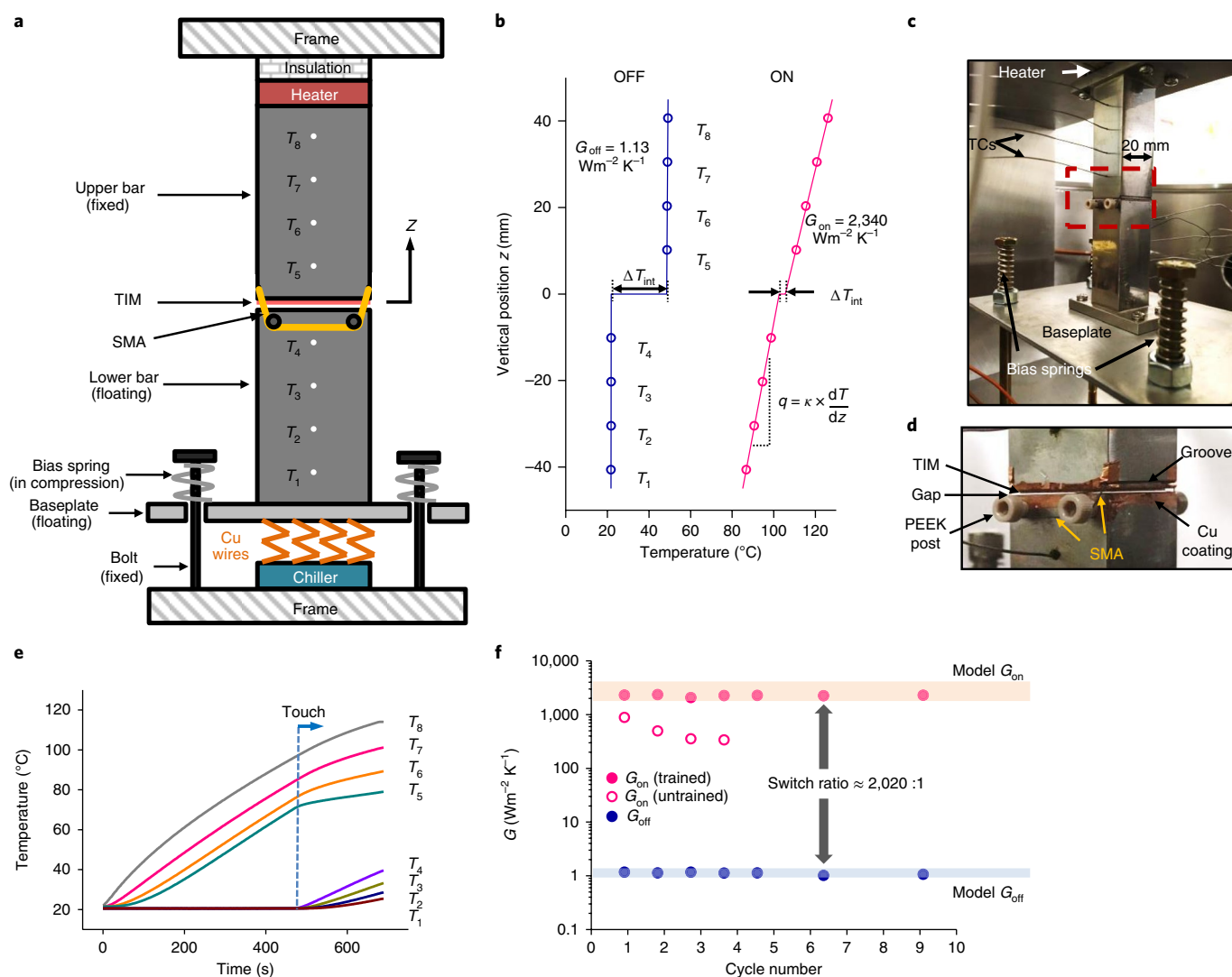
$$q = \kappa \frac{dT}{dz} \tag{3}$$

Fig. 3 | Validation of the proposed thermal regulator in a high-vacuum environment. a, Schematic of the measurement set-up. The two reference bars are made of stainless steel. Eight thermocouples (TCs) are inserted into the bars to map the temperature profile along the bars, which are used to calculate the heat flux q and temperature discontinuity ΔT_{int} at the interface. The interface thermal conductance can be immediately determined from these two quantities using equation (4). The whole upper assembly, including the upper bar and the heater, is mechanically fixed to the set-up frame and not moving. The lower bar and the baseplate attached to it are mechanically floating. The SMA wire pulls them upwards while the bias springs push them downwards. Many flexible thin Cu wires (below the baseplate) connect the lower assembly to a liquid-cooled heat sink to conduct heat away. **b**, Experimental data showing temperature profiles in the two bars for OFF (left) and ON (right) states for a single cycle, giving an SR of 2,070:1. **c**, Photo of the experimental set-up of two reference bars in a high-vacuum chamber. **d**, A close-up view of the thermal regulator region. The contacting surfaces are coated with a thin layer (~25 μm) of electroplated Cu to further improve G_{on}, as Cu is more thermally conductive and mechanically deformable than stainless steel. The Cu coating is not to be confused with the small pieces of Cu tape at the corners of the bars that are used for smoother sliding of the SMA wire. **e**, Transient temperature curves of the set-up during a start-up. The heat sink temperature is held constant at approximately 20 °C during this experiment. As soon as the heater is turned on at $t = 0$, the upper bar starts heating up, but the lower bar temperature remains flat and unaffected until the moment the two surfaces touch, which occurs when the thermal regulator temperature surpasses the critical transition temperature (≈ 70 °C). Recall that the wire temperature is close to the temperature at the lower surface of the upper bar (due to the large direct thermal contact area with the upper bar as a result of the groove), which is slightly lower than T_5. **f**, Cyclic experiments show that this thermal regulator maintains a very high switch ratio of 2,020:1 (standard deviation ±130) over the 10 cycles tested. The shaded areas indicate expected ranges of G_{on} and G_{off} from thermal models (Supplementary Information, Note 2).

The temperature discontinuity at the interface ΔT_{int} is also readily obtained by linear extrapolation of the bar temperatures. The thermal interface conductance is then simply

$$G = q/\Delta T_{int} \qquad (4)$$

Due to inevitable thermal radiation losses, the vertical heat fluxes at different locations on the reference bars are slightly different. The

lower bar has a lower temperature difference with the surrounding and less radiation loss. Therefore, the lower bar heat flux is used in equation (2) (for a detailed discussion of the data evaluation process, see Supplementary Note 3).

A Nitinol wire with a transition temperature range of around 60–80 °C is used. At temperatures below this range, the thermal regulator is thermally insulating with a vacuum gap ($D \approx 0.5$ mm) between the two surfaces (Fig. 3d). Heat can cross the gap only by

conduction through the thin SMA wires and via thermal radiation, with the latter further suppressed by the polished (down to 1,200 grit) low-emissivity metal surface (with electroplated copper). The excellent thermal isolation between the upper and lower bars in this OFF state is clearly confirmed by the very small temperature gradient in each bar (for example, $\frac{dT}{dz} = 1.8$ mK mm^{-1} in the lower bar for Fig. 3b 'OFF') and the large temperature discontinuity at the interface ($\Delta T_{int} = 26.6$ °C). When the upper bar temperature is increased above the SMA transition temperature, the wire contracts and the gap closes, enabling direct heat conduction through the TIM, and only from this moment does the lower bar start to heat up dramatically (see the transient temperature curves in Fig. 3e). Notably, this switch process occurs rapidly within around 10 s (see Supplementary Fig. 2 for temperature curve details), which is significantly faster than the tens of minutes response time reported for a linear-stroke DTE-type switch[29].

After the entire system reaches steady state in the ON condition, as shown in Fig. 3b ('ON') the temperature gradients in the reference bars are high ($\frac{dT}{dz} = 390$ mK mm^{-1}) and the discontinuity at the interface is reduced ($\Delta T_{int} = 2.9$ °C), indicating good thermal contact. The thermal interface conductance is then calculated from the steady-state data using equation (4), resulting in $G_{on} = 2,340$ Wm^{-2}K^{-1} and $G_{off} = 1.13$ Wm^{-2}K^{-1}. Therefore, a record-high room-temperature switch ratio of 2,070:1 is achieved. Furthermore, G_{on}, G_{off} and the switch ratio all fall within the ranges of prediction, confirming that both ON and OFF state heat transfer are well accounted for in the model. A total of 10 switch cycles were performed in this experiment to demonstrate the cyclability and durability.

Separate tests revealed that using SMA wire directly as-received results in poor cyclability; for example, with G_{on} decreasing by more than 60% after merely 3 cycles as shown in Fig. 3f (open circles). This is due to the well-known transformation-induced plasticity phenomenon. For this reason, all SMA wires used in the main results of Figs. 3 and 4 were first pre-conditioned using a higher stress loading, resulting in a stable, repeatable regulator response as demonstrated by the 10 cycles of Fig. 3f (filled circles, 'trained'), and the 1,000 cycles performed in the battery test presented next. See Supplementary Note 4 for more details on SMA training.

Battery thermal management demonstration

Finally, we demonstrate the potential impact of this thermal regulator using commercial LIBs in an ambient air environment (Fig. 4). Although vacuum environments for battery thermal management are technically feasible[37,38], operation in air is clearly better suited for low-cost and large-scale adoption. Only passive elements (that is, no logic control) are used in the experiments. To represent the range of climate conditions relevant to modern battery applications, the tested ambient air temperatures range from very cold (-20 °C) to very hot (45 °C)[4], which are simulated using an environmental chamber (ESPEC BTL-433, Supplementary Fig. 3). Shown in Fig. 4a,b is the test module, consisting of two Panasonic 18650PF LIBs electrically in series. The batteries are sandwiched between two aluminium holder plates to adapt their cylindrical shape to the planar thermal interface. The thermal regulator is set up between the holder and an air-cooled aluminium heat sink. This thermal regulator design is modified to fit the dimensions of the battery module, but has the same key features as our original concept shown in Fig. 2: SMA wires are in tension and adopt the 'folded' kinematic configuration to amplify stroke. Due to the larger W of this module (roughly 5 cm by 7 cm, compared to 2 cm by 2 cm for the reference bar) and the longer SMA wire length, the stroke (that is, gap size) is also larger (≈ 1 mm). The two cells' gravity force (≈ 1N) is much lower than the wire's actuation force (10–20 N); therefore, the orientation of the module does not affect its effectiveness. NiTiCu alloy, a variant of Nitinol with lower hysteresis[39], with a transition

temperature range of approximately 10–35 °C (0.010 inches diameter, Kellogg's Research Labs) is chosen for this experiment. Curved slots are created at the corners of the upper holder plate to ensure smooth sliding and to maximize heat transfer to the wires. The large majority of the wire length is above the batteries; therefore, the average wire temperature is close to the cell surface temperature.

In this practical set-up, the thermal regulator is not the only thermal resistance between the batteries and the ultimate heat sink (typically the ambient air). To reach a high system-level performance, it is critical to insulate the parallel thermal pathways, including the heat conduction through the SMA wires and springs (insignificant), and the direct convection between the cells and the ambient air, which is largely suppressed by an aerogel blanket (Fig. 4a). Similarly, series thermal resistances, such as the interface resistance between the cells and the holder plate, need to be minimized. A simple thermal circuit model is presented in Supplementary Note 5 to analyse the effects of parallel and series thermal resistances in this battery experiment.

To compare the performance of the thermal regulator with traditional linear, non-switched BTMS components, we also conducted control experiments for two reference conditions: 'always ON' and 'always OFF'. These are achieved by replacing the SMA wires with stainless steel dummy wires adjusted to give either an intimate interface ('always ON') or an open gap (≈ 1 mm, 'always OFF'), respectively. The thermal regulator and the two control configurations are tested with standard discharging cycles at 2C rate with the results presented in Fig. 4.

At a very low $T_{ambient}$ of -20 °C, batteries lose a large fraction of their capacity if not warmed up quickly, which is exactly what is seen for the 'always ON' case (only 21% rated capacity) in Fig. 4c due to continuous heat dissipation through the intimate thermal contact. In contrast, for both the 'always OFF' and the thermal regulator cases of Fig. 4c, the temperature of the battery module rises rapidly to around 20 °C because leakage of self-generated heat is blocked by the air gap. As a result, the usable capacity of the batteries is increased by more than a factor of three. The thermal regulator case delivers slightly less thermal insulation and lower capacity (76% versus 89% rated capacity) compared with 'always OFF', due to the gap size decreasing above 10 °C. If needed, the off-state gap size can be easily increased by extending the lateral wire routing (that is, increasing the effective W in equation (2)). Not only do the regulated batteries heat up more quickly compared to the default 'always ON' design, they also cool down significantly more slowly as shown in Fig. 4e. It takes 20 min before the module temperature drops back below -10 °C in the presence of the thermal regulator, which is beneficial for dynamic EV drive cycles in winter that include brief stops.

Although the 'always OFF' BTMS strategy had its merits at low temperatures, it is unacceptable for high-temperature environments because it blocks heat dissipation when the batteries need to be cooled. Figure 4d compares the performance of all three strategies for a hot environment ($T_{ambient} = 45$ °C). The discharge capacity is close to (actually slightly higher than) the rated capacity because of the high temperature for all three cases. However, the module temperature with an 'always OFF' strategy increases by 20 °C to an unsafe level of 65 °C (the maximum allowed temperature is 60 °C according to the manufacturer's data sheet, while the Department of Energy target is 52 °C; ref. [7]). Such high temperatures accelerate the battery degradation and increase the risk of thermal runaway[6,40,41]. At the same time, it is clear that the thermal regulator has become thermally conducting at this temperature, enabling efficient cooling of the module and limiting the temperature rise to around 5 °C. Indeed, the thermal regulator's cooling performance approaches that of the 'always ON' reference device, as expected.

In addition to these experiments at -20 °C and 45 °C, we have also exercised the battery module with the thermal regulator at
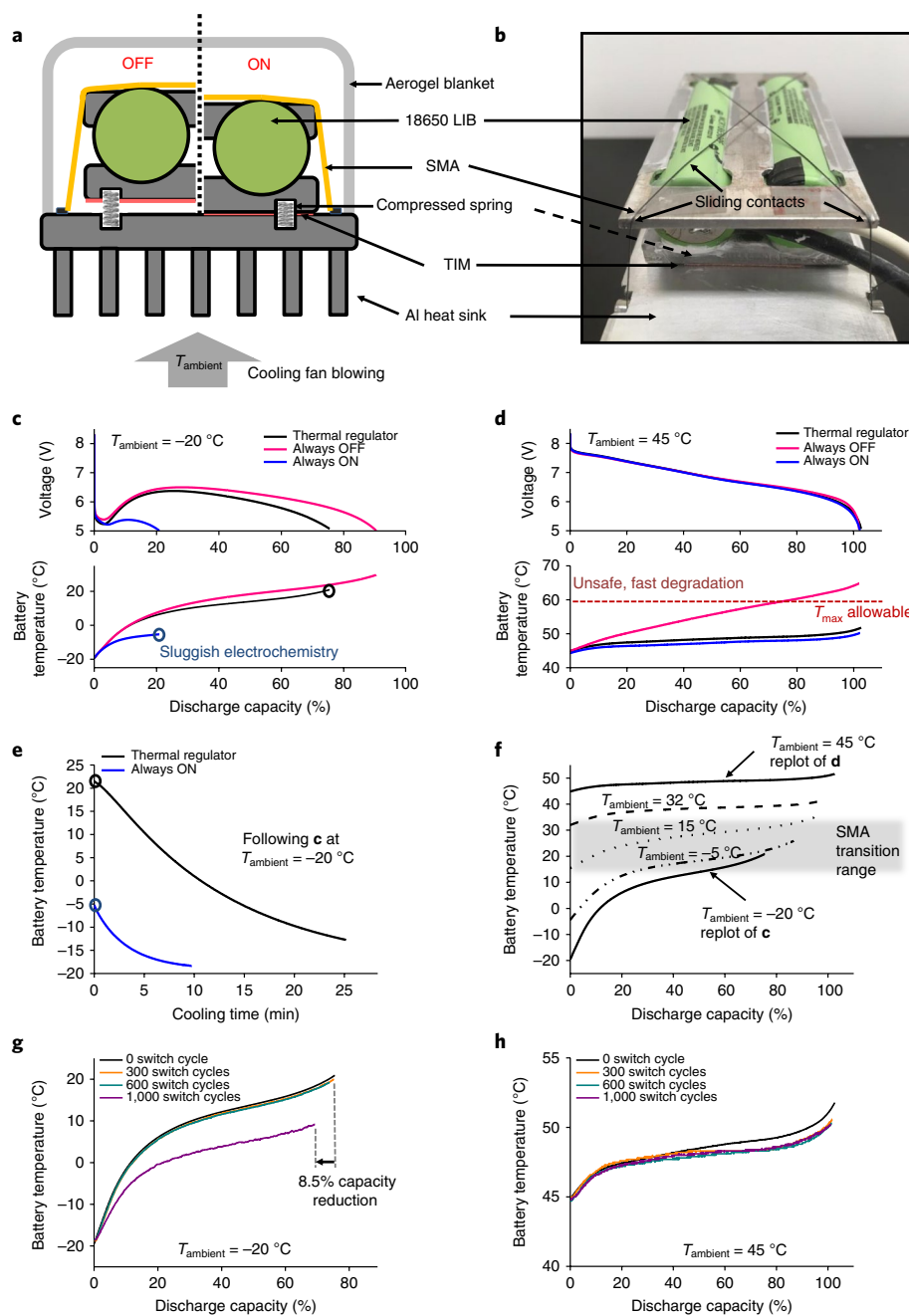
Fig. 4 | Demonstration of the thermal regulator with a module of two commercial 18650 LIBs. a, A schematic of the experimental set-up; a split view showing the OFF and ON states. Two Panasonic 18650PF cells are sandwiched between holder plates and the whole assembly is attached to an air-cooled heat sink through a thermal regulator, which provides an air gap at low temperatures and intimate thermal contact at high temperatures. Two thermocouples (not shown) are attached to the exposed side walls of the two cells to measure the battery temperature. Both of their readings are in close agreement ($\pm 1 °C$), and their average is presented in the following plots. **b**, Photo of the test assembly. **c,d**, Comparison of battery performance with the thermal regulator, always ON and always OFF for representative cold ($-20 °C$, (**c**)) and hot ($45 °C$, (**d**)) ambient temperatures. For each test, the battery module is fully charged and then the entire test assembly is allowed to come to thermal equilibrium with $T_{ambient}$ before discharging at a 2C rate. The charging and discharging cutoff voltages are $4.2 V$ and $2.5 V$ per cell, respectively, and the two cells are electrically in series. Measured discharge capacity is calculated as a percentage of the rated capacity, 2,700 mAh per cell. For a cold environment as in **c**, the thermal regulator becomes thermally insulating to retain battery-generated heat. Compared with the common 'always ON' design, $T_{battery}$ rises much higher ($\Delta T_{battery}$ of $40 °C$ versus $15 °C$) and the usable capacity more than triples. For a hot environment as in **d**, the thermal regulator becomes thermally conducting to dissipate heat and prevent the batteries from overheating. As a comparison, the 'always OFF' design, which performed well at low temperature, now results in the batteries heating to unsafe levels. Together these two panels show how the thermal regulator adapts to the ambient environment and regulates battery temperature passively without external stimuli or energy input. **e**, Transient temperature responses during free cooling after the discharge cycle is completed at $-20 °C$, immediately following the same two curves shown in **c**. **f**, Temperatures of the battery module equipped with the thermal regulator discharged at five different ambient temperatures. **g,h**, Investigating cyclability of the thermal regulator at $T_{ambient} = -20 °C$ and $T_{ambient} = 45 °C$, respectively. The thermal regulator was taken through 1,000 switching cycles by directly heating the SMA wire (5 s ON/10 s OFF). In addition, the battery module performance was tested using the same procedure as in **c** and **d** at four stages: before switch cycling and after 300, 600 and 1,000 switch cycles.

several intermediate $T_{ambient}$ values, with the results given in Fig. 4f. The gradual transition from completely OFF at −20 °C to completely ON at 45 °C can be seen. This transition is further confirmed by additional experiments using cartridge heaters to provide constant power (details in Supplementary Note 6). Hence, the thermal regulator has successfully achieved its objective of thermally insulating the module at low temperatures and cooling the module at high temperatures, as initially envisioned in Fig. 1. This thermal functionality is impossible with traditional linear thermal elements. Meanwhile, the thermal regulator demonstrated robust performance under abuse conditions including a 5C rate at high temperature and temporary short-circuit (see Supplementary Note 7).

The calendar ageing and cyclability of the thermal regulator with the battery module was also tested. After the initial performance characterization (Fig. 4c–f), the module was left on a bench in laboratory air for six months. Subsequently, we placed the test module in $T_{ambient}$ of −20 °C and switched the regulator by directly Joule heating the SMA wires to close and open the gap. For an EV automotive application, we anticipate that this thermal regulator would go through a switch cycle (OFF to ON to OFF) every time the battery is charged in cold climates, and less frequently in mild and hot climates, which require good heat sinking at all times. The 18650 cells' cycle life is roughly 500 cycles at 100% depth of discharge[42] and is longer at lower depth of discharge[43]. Considering these factors, we performed 1,000 switch cycles on the thermal regulator as a durability test. As shown in Fig. 4g, the thermal regulator's 'OFF' state performances is very well preserved over the 6-month ageing and 600 switch cycles, degrading slightly after 1,000 cycles to result in an 8.5% battery capacity reduction at −20 °C. The thermal regulator's 'ON' state performance was not compromised even after 1,000 thermal cycles, with the maximum temperature increasing by less than 1 °C. In a real outdoor environment, dust particles are expected to be a threat to the thermal contact and on-state performance. Therefore, the thermal regulator would probably require a hermetic seal to maintain this level of cyclic stability.

From a systems integration perspective, compared to a standard 'always-ON' BTMS approach, the minimal additional hardware requirements to implement this thermal regulator are in principle only the bias springs and the SMA wire; we note that a TIM is already required in an 'always-ON' BTMS to bridge the cells to the heat sink, and the functionality of the holder plates of Fig. 4a,b might be omitted for prismatic cells with flat surfaces or incorporated into existing heat sinks with curved surfaces already used to secure cylindrical cells. In the best case considering only the SMA wire and bias springs, the additional mass is less than 1 g, which is minimal compared to the mass of two 18650 cells (92 g). Similarly, the material cost of Nitinol (0.08 g at US$30–300 kg^{-1}) is also significantly less than 1% of the battery cost (approximately US$6)[2]. The thermal regulator is expected to be compatible with other types of cell and pack size (Supplementary Note 8).

Conclusions

We have presented a passive thermal regulator to address the critical need for adaptive thermal management in battery applications. Demonstration with a battery module consisting of commercial 18650 lithium-ion cells shows that this thermal regulator increases cold-weather capacity by more than threefold simply by retaining the battery's self-generated heat (even larger effects should be accessible through intentional self-heating such as in refs [13,14]) while also keeping the module from overheating in hot environments even at a high 2C discharge rate. We anticipate that this study may point the way towards a simpler and more energy-efficient approach to the thermal management of batteries in a wide range of climates, which is important for faster adoption of EVs and battery-based energy storage, with potentially broader impacts on battery-critical applications such as drones and portable electronics. In addition, this study showcases how thermally functional materials and devices[20] enable new thermal management strategies that have not been possible previously.

Methods

Reference bar experiments. Reference bars are machined to a tolerance of 25 μm. The contacting surfaces are polished using sandpapers from 220 down to 1,500 grit sizes. K type thermocouples of 254 μm (0.010 inches) diameter are used for measuring the temperature profile and the data are logged by a Keithley 2700 acquisition system. A custom common cold junction is made by sandwiching all of the thermocouples' cold ends between two Al blocks and connecting the cold junction and Keithley terminals using Cu wires. The experiments take place in a bell jar with vacuum level better than 10^{-5} torr. For steady-state measurements, we allow 5–20 h for the system to stabilize before the temperature data are recorded.

Battery thermal regulator experiments. Al alloy 6061 is used to construct the holder plates and the heat sink. The slots accommodating the cells are machined and then polished to 1,500 grit. Silicone grease is used to reduce the thermal interface resistance between the cells and the holder plates. The battery module is cycled with a PEC Corp SBT2050 tester in an ESPEC BTL-433 environmental chamber.

Data availability

The data that support the plots within this paper and other findings of this study are available from the corresponding author upon reasonable request.

References

1. Dunn, B., Kamath, H. & Tarascon, J. M. Electrical energy storage for the grid: a battery of choices. *Science* **334**, 928–935 (2011).
2. Nykvist, B. & Nilsson, M. Rapidly falling costs of battery packs for electric vehicles. *Nat. Clim. Change* **5**, 329–332 (2015).
3. Chu, S., Cui, Y. & Liu, N. The path towards sustainable energy. *Nat. Mater.* **16**, 16–22 (2017).
4. Yuksel, T. & Michalek, J. J. Effects of regional temperature on electric vehicle efficiency, range, and emissions in the United States. *Environ. Sci. Technol.* **49**, 3974–3980 (2015).
5. Wang, Q., Jiang, B., Li, B. & Yan, Y. A critical review of thermal management models and solutions of lithium-ion batteries for the development of pure electric vehicles. *Renew. Sust. Energ. Rev.* **64**, 106–128 (2016).
6. Pesaran, A. A., Santhanagopalan, S. & Kim, G. H. Addressing the impact of temperature extremes on large format Li-ion batteries for vehicle applications. *30th Int. Battery Seminar* PR-5400-58145 (2013).
7. Keyser, M. et al. Enabling fast charging–battery thermal considerations. *J. Power Sources* **367**, 228–236 (2017).
8. Ebner, M., Marone, F., Stampanoni, M. & Wood, V. Visualization and quantification of electrochemical and mechanical degradation in Li ion batteries. *Science* **342**, 716–720 (2013).
9. Leng, F., Tan, C. M. & Pecht, M. Effect of temperature on the aging rate of Li ion battery operating above room temperature. *Sci. Rep.* **5**, 12967 (2015).
10. Jaguemont, J., Boulon, L. & Dubé, Y. A comprehensive review of lithium-ion batteries used in hybrid and electric vehicles at cold temperatures. *Appl. Energy* **164**, 99–114 (2016).
11. *Maximizing Battery Life and Lifespan* (Apple, accessed 1 March 2018); https://www.apple.com/batteries/maximizing-performance
12. Arguez, A. et al. NOAA's 1981–2010 US climate normals: an overview. *Bull. Am. Meteor. Soc.* **93**, 1687–1697 (2012).
13. Ji, Y. & Wang, C. Y. Heating strategies for Li-ion batteries operated from subzero temperatures. *Electrochim. Acta* **107**, 664–674 (2013).
14. Wang, C. Y. et al. Lithium-ion battery structure that self-heats at low temperatures. *Nature* **529**, 515 (2016).
15. Zhang, G. et al. Rapid restoration of electric vehicle battery performance while driving at cold temperatures. *J. Power Sources* **371**, 35–40 (2017).
16. Buford, K., Williams, J. & Simonini, M. *Determining Most Energy Efficient Cooling Control Strategy of a Rechargeable Energy Storage System* Report 0148-7191 (SAE Technical Paper, 2011).
17. Novak, K. S., Phillips, C. J., Sunada, E. T. & Kinsella, G. M. *Mars Exploration Rover Surface Mission Flight Thermal Performance* Report 0148-7191 (SAE Technical Paper, 2005).
18. Ando, M., Shinozaki, K., Okamoto, A., Sugita, H. & Nohara, T. Development of mechanical heat switch for future space missions. *Proc. 44th Int. Conf. Environ. Syst.* (2014).
19. Shu, Q., Demko, J. & Fesmire, J. Heat switch technology for cryogenic thermal management. *IOP Conference Series Mater. Sci. Engin.* 012133 (IOP Publishing, 2017).

20. Wehmeyer, G., Yabuki, T., Monachon, C., Wu, J. & Dames, C. Thermal diodes, regulators, and switches: Physical mechanisms and potential applications. *Appl. Phys. Rev.* **4**, 041304 (2017).
21. Lyeo, H. K. et al. Thermal conductivity of phase-change material $Ge_2Sb_2Te_5$. *Appl. Phys. Lett.* **89**, 151904 (2006).
22. Reifenberg, J. P. et al. Thickness and stoichiometry dependence of the thermal conductivity of GeSbTe films. *Appl. Phys. Lett.* **91**, 111904 (2007).
23. Zhu, J. et al. Temperature-gated thermal rectifier for active heat flow control. *Nano Lett.* **14**, 4867–4872 (2014).
24. Ito, K., Nishikawa, K., Iizuka, H. & Toshiyoshi, H. Experimental investigation of radiative thermal rectifier using vanadium dioxide. *Appl. Phys. Lett.* **105**, 253503 (2014).
25. Ben-Abdallah, P. & Biehs, S. A. Phase-change radiative thermal diode. *Appl. Phys. Lett.* **103**, 191907 (2013).
26. Yang, J. et al. Enhanced and switchable nanoscale thermal conduction due to van der Waals interfaces. *Nat. Nanotech.* **7**, 91–95 (2012).
27. Cho, J. et al. Electrochemically tunable thermal conductivity of lithium cobalt oxide. *Nat. Commun.* **5**, 4035 (2014).
28. Ihlefeld, J. F. et al. Room-temperature voltage tunable phonon thermal conductivity via reconfigurable interfaces in ferroelectric thin films. *Nano Lett.* **15**, 1791–1795 (2015).
29. Guo, L., Zhang, X., Huang, Y., Hu, R. & Liu, C. Thermal characterization of a new differential thermal expansion heat switch for space optical remote sensor. *Appl. Therm. Eng.* **113**, 1242–1249 (2017).
30. Marland, B., Bugby, D. & Stouffer, C. Development and testing of an advanced cryogenic thermal switch and cryogenic thermal switch test bed. *Cryogenics* **44**, 413–420 (2004).
31. Jani, J. M., Leary, M., Subic, A. & Gibson, M. A. A review of shape memory alloy research, applications and opportunities. *Mater. Des.* **56**, 1078–1113 (2014).
32. Jain, A. & Goodson, K. E. Measurement of the thermal conductivity and heat capacity of freestanding shape memory thin films using the 3ω method. *J. Heat Transfer* **130**, 102402 (2008).
33. Yovanovich, M. M. Four decades of research on thermal contact, gap, and joint resistance in microelectronics. *IEEE Trans. Components Packaging Technol* **28**, 182–206 (2005).
34. Tso, C. Y. & Chao, C. Y. Solid-state thermal diode with shape memory alloys. *Int. J. Heat Mass Transfer* **93**, 605–611 (2016).
35. Saums, D. *ASTM D 5470-06 Thermal Interface Material Test Stand* (DS&A LLC, 2006).
36. Hao, M., Saviers, K. R. & Fisher, T. S. Design and validation of a high-temperature thermal interface resistance measurement system. *J. Therm. Sci. Eng. Appl.* **8**, 031008 (2016).
37. Aceves, S. M., Berry, G. D., Martinez-Frias, J. & Espinosa-Loza, F. Vehicular storage of hydrogen in insulated pressure vessels. *Int. J. Hydrogen Energy* **31**, 2274–2283 (2006).
38. Kuze, Y., Kobayashi, H., Ichinose, H. & Otsuka, T. *Development of New Generation Hybrid System (THS II)-Development of Toyota Coolant Heat Storage System* Report 0148-7191 (SAE Technical Paper, 2004).
39. Strnadel, B., Ohashi, S., Ohtsuka, H., Ishihara, T. & Miyazaki, S. Cyclic stress-strain characteristics of TiNi and TiNiCu shape memory alloys. *Mater. Sci. Eng. A* **202**, 148–156 (1995).
40. Santhanagopalan, S., Zhang, Q., Kumaresan, K. & White, R. E. Parameter estimation and life modeling of lithium-ion cells. *J. Electrochem. Soc.* **155**, A345–A353 (2008).
41. Ramadass, P., Haran, B., Gomadam, P. M., White, R. & Popov, B. N. Development of first principles capacity fade model for Li-ion cells. *J. Electrochem. Soc.* **151**, A196–A203 (2004).
42. Panasonic 18650PF Specifications (Panasonic, accessed 20 July 2018); https://industrial.panasonic.com/ww/products/batteries/secondary-batteries/lithium-ion/cylindrical-type
43. Millner, A. Modeling lithium ion battery degradation in electric vehicles. In *Proc. 2010 IEEE Conference Innovative Technol. Efficient Reliable Electricity Supply (CITRES)* 349–356 (IEEE, 2010).

Author contributions
M.H. and C.D. conceived and designed the experiments. M.H. and J.L. conducted the proof-of-concept test in vacuum. M.H., S.P. and S.M. performed the experiments with the battery module. M.H. and C.D. co-wrote the paper. All authors discussed the results and commented on the manuscript.

Competing interests
M.H. and C.D. are co-inventors on a provisional patent application (US 62/719,220) that has been filed by the Regents of the University of California based on this work.

Additional information
Supplementary information is available for this paper at https://doi.org/10.1038/s41560-018-0243-8.

Reprints and permissions information is available at www.nature.com/reprints.

Correspondence and requests for materials should be addressed to C.D.

Publisher's note: Springer Nature remains neutral with regard to jurisdictional claims in published maps and institutional affiliations.